NANO LETTERS

Letter

pubs.acs.org/NanoLett

Atomic-Scale Snapshots of the Formation and Growth of Hollow PtNi/C Nanocatalysts

Raphaël Chattot,[†,‡] Tristan Asset,[†,‡] Jakub Drnec,[§] Pierre Bordet,[∥,⊥] Jaysen Nelayah,[#] Laetitia Dubau,*[,†,‡] and Frédéric Maillard*[,†,‡]

[†]Univ. Grenoble Alpes, LEPMI, F-38000 Grenoble, France

[‡]CNRS, LEPMI, F-38000 Grenoble, France

[§]European Synchrotron Radiation Facility, ID 31 Beamline, BP 220, F-38043 Grenoble Cedex, France

[∥]Université Grenoble Alpes, Institut Néel, F-38000 Grenoble, France

[⊥]CNRS, Institut Néel, F-38000 Grenoble, France

[#]Université Paris Diderot, Sorbonne Paris Cité, CNRS, Laboratoire Matériaux et Phénomènes Quantiques, UMR 7162, F-75013, Paris, France

Supporting Information

ABSTRACT: Determining the formation and growth mechanism of bimetallic nanoparticles (NPs) with atomic detail is fundamental to synthesize efficient "catalysts by design". However, an understanding of the elementary steps which take place during their synthesis remains elusive. Herein, we have exploited scanning transmission electron microscopy coupled to energy-dispersive X-ray spectroscopy, operando wide angle and small-angle X-ray scattering, and electrochemistry to unveil the formation and growth mechanism of hollow PtNi/C NPs. Such NPs, composed of a PtNi shell surrounding a nanoscale void, catalyze efficiently and sustainably the oxygen reduction reaction (ORR) in an acidic electrolyte. Our step-by-step study reveals that (i) Ni-rich/C NPs form first, before being embedded in a $Ni_xB_yO_z$ shell, (ii) the combined action of galvanic displacement and the nanoscale Kirkendall effect then results in the sequential formation of Ni-rich core@Pt-rich/C shell and ultimately hollow PtNi/C NPs. The electrocatalytic properties for the ORR and the stability of the different synthesis intermediates were tested and structure−activity−stability relationships established both in acidic and alkaline electrolytes. Beyond its interest for the ORR electrocatalysis, this study also presents a methodology that is capable to unravel the formation and growth mechanism of various nanomaterials including preferentially shaped metal NPs, core@shell NPs, onion-like NPs, Janus NPs, or a combination of several of these structures.

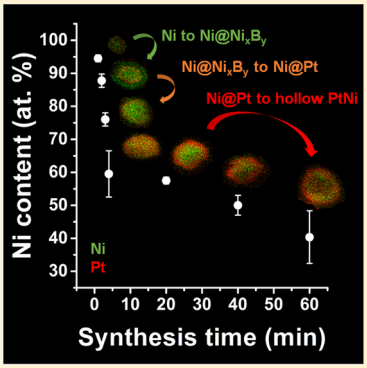

KEYWORDS: *Operando identification of synthesis intermediates, hollow PtNi NPs, nanoscale Kirkendall effect, galvanic replacement, oxygen reduction reaction*

The electrocatalytic properties of bimetallic nanoparticles (NPs) are strongly affected by their atomic arrangement. This holds especially true in proton-exchange membrane fuel cells (PEMFC) where enhanced oxygen reduction reaction (ORR) kinetics has been measured for specific chemical compositions and shapes of PtM alloys (M being an early or late transition metal) or M-rich core@Pt-rich shell NPs.[1−6] In that respect, step-by-step characterizations of the different nanostructures formed during the synthesis of alloyed NPs and their time-sequenced evolution are not only fundamental in terms of scientific knowledge but also provide leverage for controlling the spatial distribution of the metal atoms and thus rationalizing their catalytic activity at the atomic scale. Using this approach, Cui et al.[3] recently reported that, during the growth of PtNi octahedra, a branched Pt-rich structure forms first onto which Ni atoms are preferentially deposited, resulting into Pt-enriched apexes and Ni-rich facets. Using a different solvent (hexane), Chen et al.[4] have shown that the Ni-rich facets may be slowly etched to form porous PtNi nanoframes.

Bimetallic hollow NPs, another class of highly active (electro)catalysts for the ORR (a 9-fold enhancement in specific activity for the ORR and a 6-fold enhancement in mass activity for the ORR, were recently reported on hollow PtNi/C NPs by Dubau et al.,[7−10] in agreement with results of other groups[11−15]) could also benefit from the detailed knowledge of the synthesis steps. Yin et al.[16] have shown that the nanoscale Kirkendall effect (an interdiffusion process into a bimetallic alloy or a core@shell material driven by the difference in the interdiffusion coefficients of the two elements and resulting into the entrance of atomic vacancies inside the material) is

Received: January 10, 2017
Revised: March 15, 2017
Published: March 24, 2017

DOI: 10.1021/acs.nanolett.7b00119
Nano Lett. 2017, 17, 2447−2453

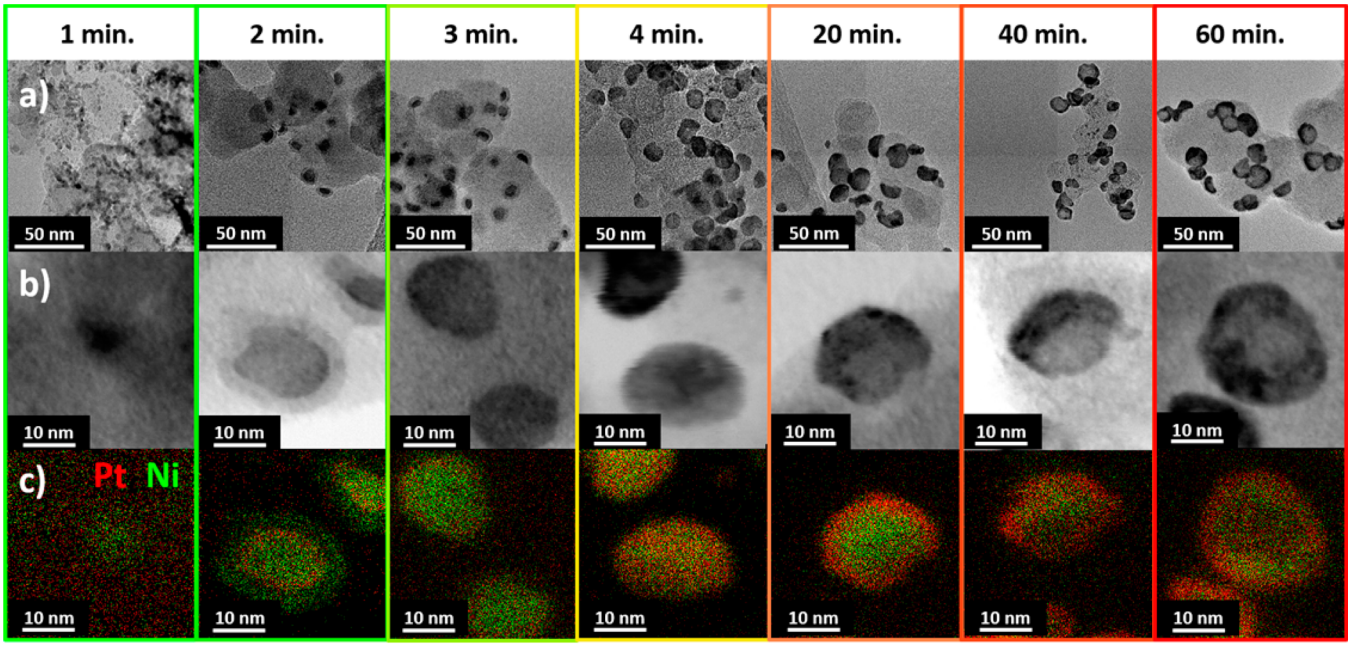

Figure 1. Time-sequenced formation and growth of hollow PtNi/C nanoparticles by electron and X-ray based techniques. (a) Conventional, (b) scanning transmission electron microscopy images, and (c) X-ray energy dispersive spectroscopy elemental maps of the different nanostructures forming during the synthesis of hollow PtNi/C NPs.

responsible for the spontaneous formation of hollow Co_3S_4 or CoO NPs upon exposure to elemental S or O_2 atmospheres, respectively. Combined sequentially or in series with galvanic replacement (a spontaneous electrochemical process in which the oxidation of a metal phase provides electrons to reduce the ions of another metal having a higher standard potential), the nanoscale Kirkendall effect has now become a simple and versatile route to bimetallic hollow NPs composed of a noble element (typically gold—Au or platinum—Pt) and a less-noble element (typically silver—Ag, palladium—Pd, cobalt—Co or nickel—Ni), which acts as an anode during galvanic replacement (sacrificial template).[5,17−22] Factors consisting of (i) the nature of the sacrificial element,[22] (ii) the stoichiometry between the more noble and the less noble elements,[10,14] (iii) the temperature at which the synthesis is performed (the interdiffusion coefficient of the elements strongly depends on the temperature[23]), and (iv) the shape of the sacrificial template[18,22] provide control over the chemical composition, the elemental distribution, the size, and the shape of the final hollow NPs.

However, to date, the details and the kinetics of formation and growth of hollow nanocatalysts are still elusive. Moreover, the (electro)catalytic activities and the stability of the different nanostructures forming during the synthesis are unknown and need to be unravelled. Herein, using a unique combination of operando synchrotron wide- and small-angle X-ray scattering (WAXS and SAXS, respectively), aberration-corrected high-resolution transmission electron microscopy (HR-TEM), scanning transmission electron microscopy (STEM), energy-dispersive X-ray photoelectron spectroscopy (X-EDS), X-ray spectroscopy (XPS), and electrochemical techniques, we address these issues on hollow PtNi/C nanocatalysts.

Methodology. Hollow PtNi/C NPs were synthesized by a one-pot process in which $Pt(NH_3)_4Cl_2{\cdot}(H_2O)$ and $NiCl_2$ were first dissolved in deionized water, mixed with Vulcan XC72 (a high surface carbon support), and reduced by dropwise addition of a sodium borohydride ($NaBH_4$) solution under vigorous magnetic stirring and air atmosphere.[10] Different electron or X-ray-based techniques were used to unravel the nature of the different nanostructures forming during the synthesis. For analyses with electron-based techniques, the synthesis was conducted in a glass reactor, and a peristaltic pump was used to add the $NaBH_4$ solution in a dropwise manner. Sampling was performed in the reactor at t = 0, 1, 2, 3, 4, 5, 7, 10, 20, 40, and 60 min after the addition of the first drop of the $NaBH_4$ solution. The aliquots were then deposited onto TEM grids, and the chemical reactions at stake were stopped by drying as fast as possible with a heat gun. Operando WAXS and SAXS measurements were performed at ID31 beamline of the European Synchrotron Radiation Facility (ESRF). The same experimental protocol was used, but a poly(methyl methacrylate) cuvette served as reactor, and the $NaBH_4$ solution was added using a remote controlled syringe. Finally, for electrochemical measurements, the synthesis was performed in a glass reactor and catalytic powder was collected at different time intervals and then filtered and rinsed with deionized water as fast as possible. All other details on the synthesis, materials and methods are presented in the Supporting Information (SI).

Atomic-Scale Morphological Changes Occurring during the Synthesis of Hollow PtNi/C NPs. Conventional transmission electron microscopy (TEM) and STEM images as well as X-EDS elemental maps of the nanostructures formed after 1, 2, 3, 4, 20, 40, and 60 min are displayed in Figure 1. HR-TEM images and particle size distributions of the different synthesis intermediates are provided in Figures S1, S2, and S3 in the SI, respectively. The X-EDS elemental maps show that the reduction of the metal salts by $NaBH_4$ is extremely fast. In the time period $0 < t \leq 1$ min, Ni^{2+} ions are preferentially reduced according to eq 1:

$$2Ni^{2+}(aq) + BH_4^-(aq) + 2H_2O(l) \rightarrow 2Ni(s) + BO_2^-(aq) + 4H^+(aq) + 2H_2(g) \quad (1)$$

DOI: 10.1021/acs.nanolett.7b00119
Nano Lett. 2017, 17, 2447−2453

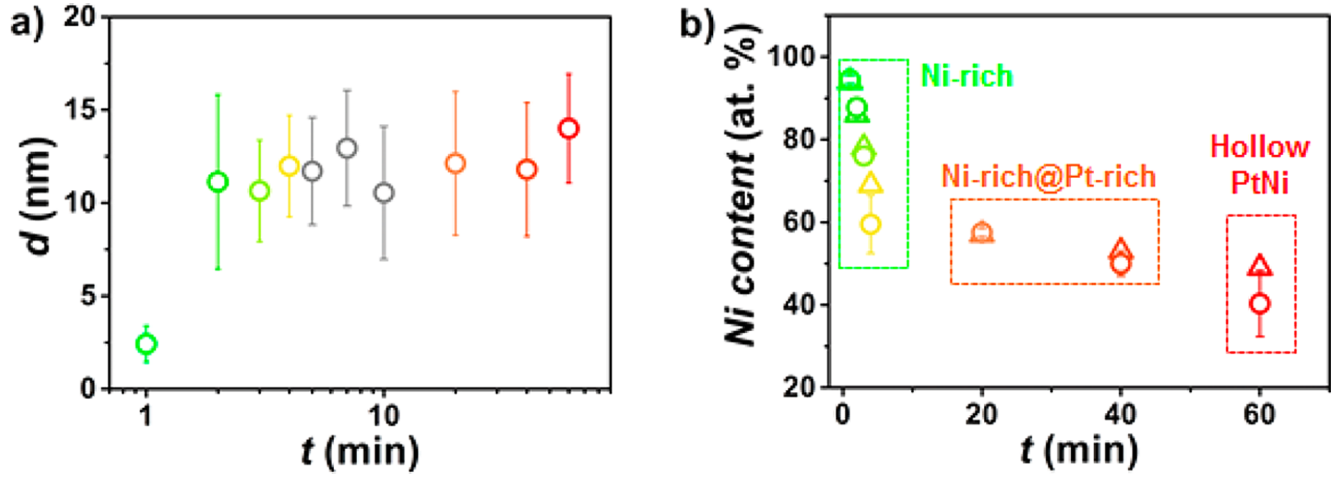

Figure 2. Structural and chemical changes occurring during the synthesis of the hollow PtNi/C nanoparticles. Variation of (a) the external diameter and (b) the Ni content of the NPs. The external diameter was approximated by counting between 100 and 250 nanoparticles at each stage (see Table S2 in the SI). The triangles represent the Ni content measured on individual NPs by STEM-XEDS and the circles the average chemical composition measured on hundreds of NPs (by X-EDS on low-magnification TEM images). For both measurements, the error bar is the standard deviation.

The preferential reduction of Ni^{2+} ions by $NaBH_4$ is surprising in view of the more negative standard potential of Ni^{2+}/Ni (E^0 = −0.26 V vs the standard hydrogen electrode, SHE) relative to the $Pt(NH_3)_4^{2+}/Pt$ (E^0 = 0.62 V vs SHE) and Pt^{2+}/Pt (E^0 = 1.19 V vs SHE) redox couples.[24] However, it may be rationalized by considering the nature of the Pt salt precursor. Indeed, $[Pt(NH_3)_4]^{2+}$ is inert (opposite to labile), i.e., slowly decomposes in water, which allows for the sequential deposition of Ni atoms and then of Pt atoms. In contrast, due to faster decomposition kinetics in water, solid alloy PtNi/C NPs are formed when $PtCl_6^{2-}$ ions are used.[14]

The Ni/C NPs are then rapidly ($1 < t \leq 2$ min) embedded into a matrix composed of Ni atoms and one or several lighter element(s) as illustrated by the strong contrast between the core of the NPs and their surface and near-surface region in the STEM images (Figure 1). XPS measurements revealed that the shell forming at the surface is composed of nickel borides (Ni_xB_y, see Figures S4 and S5 and Table S1 in the SI). This result is in line with the affinity of boron (B) with most of the transition metal elements and the associated spontaneous formation of transition metal borides as documented in literature.[25−34] Nickel borides (NiB, Ni_2B, Ni_3B, and NiB_3 are the most common phases obtained via the reduction of Ni^{2+} ions in BH_4^--containing solution[34−39]) may form by reacting with the $NaBH_4$ solution according to eq 2 and eq 3, respectively:

$$2Ni^{2+}(aq) + 4BH_4^-(aq) + 6H_2O(l) \rightarrow Ni_2B(s) + 3BO_2^-(aq) + 3H^+ + 12.5H_2(g) \quad (2)$$

$$6Ni^{2+}(aq) + 5BH_4^-(aq) + 6H_2O(l) \rightarrow 2Ni_3B(s) + 3BO_2^-(aq) + 10H^+ + 11H_2(g) \quad (3)$$

Note that the Ni_xB_y shell also contains oxygen (O) atoms as shown by the presence of the Ni $2p_{3/2}$ satellite peak at 859.3 eV in XP spectra, which may correspond to $Ni(OH)_2$ or NiO and the ca. 5 eV positive shift of the B 1s binding energy (about 5 eV) relative to elemental boron.[40,41] $Ni(BO_2)_2$ phases are formed by the reaction between BO_2^- ions produced by Ni^{2+} reduction (eq 1, eq 2 and eq 3) or homogeneous hydrolysis of the $NaBH_4$ solution (eq 4):

$$BH_4^-(aq) + 2H_2O(l) \rightarrow BO_2^-(aq) + 4H_2(g) \quad (4)$$

$$Ni^{2+}(aq) + 2BO_2^-(aq) \rightarrow Ni(BO_2)_2 \quad (5)$$

STEM/X-EDS images recorded in the time period $2 < t \leq 20$ min show that the surface of the Ni-rich core@$Ni_xB_yO_z$ shell/C nanostructures enriches in Pt, resulting in the formation of Ni-rich core@Pt-rich shell/C NPs after 20 min. Pt atoms are deposited at the surface of the growing NPs via galvanic replacement (the $Ni_xB_yO_z$ shell covering the Ni-rich cores is oxidized while $Pt(NH_3)_4^{2+}$ ions are reduced) or chemical reduction by hydrogen (H_2) molecules and BH_4^- ions present in solution.

Finally, a slow transformation of the solid Ni-rich core@Pt-rich shell NPs into alloyed hollow PtNi/C NPs is observed from $20 < t < 60$ min. This structural evolution is caused by the gradient in chemical potential between Pt and Ni atoms in the core@shell nanostructure, and their different degrees of oxophilicity. Both act as strong driving forces for Ni atoms to interdiffuse to the surface. Moreover, since Ni atoms interdiffuse outward more rapidly than Pt atoms inward, atomic vacancies enter the nanomaterial and condensate into voids yielding ultimately hollow PtNi/C NPs. This phenomenon is known as the nanoscale Kirkendall effect.[22,42]

The changes of the external diameter of the NPs and of their Ni content are represented in Figure 2. They suggest that galvanic displacement occurs mainly during the first 4 min of the synthesis (fast variation of the Ni content), while smoother variations of these two parameters at $t > 4$ min are caused by the slower nanoscale Kirkendall effect. XPS measurements conducted on the different synthesis intermediates confirmed this scenario (Figure S5).

Structural Changes Occurring during the Synthesis of Hollow PtNi/C NPs. Complementary to electron-based techniques, operando WAXS measurements were carried out to probe the structure of the synthesis intermediates at a larger scale. Despite the strong H_2 evolution arising from the reduction of Ni^{2+} ions (eq 1), and the homogeneous hydrolysis of the $NaBH_4$ solution (eq 4), the WAXS patterns of the growing PtNi/C nanocrystallites could be recorded (Figure 3a). The first reflections, observed at $2\theta \sim 4.5°$, were ascribed to the formation of Ni_xB_y phases in agreement with ref 39. For $3 < t <$

DOI: 10.1021/acs.nanolett.7b00119
Nano Lett. 2017, 17, 2447−2453

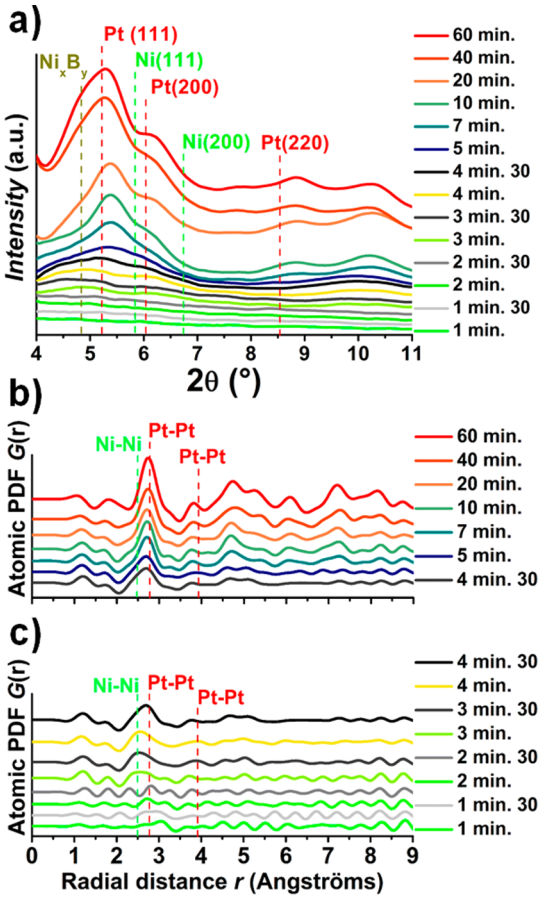

Figure 3. Structural characterization of the different nanostructures forming during the synthesis of hollow PtNi/C nanoparticles. (a) High-energy WAXS patterns (the vertical dashed lines indicate the reflections of pure metallic Pt and Ni) and (b, c) experimental atomic pair distribution functions.

5 min, patterns typical of X-ray diffraction from Ni(111), Pt(111), and Pt(200) planes were observed at $2\theta \sim 6.0°$, $2\theta \sim 5.3°$, and $2\theta \sim 5.8°$, respectively. The reflections ascribed to Pt increased in intensity at longer times, indicating enrichment in Pt in agreement with the STEM/X-EDS elemental maps displayed in Figure 1. The reflections also shifted to larger 2θ values, suggesting that the PtNi lattice parameter relaxed toward the value of pure Pt.

The experimental pair distribution functions (PDF) extracted from the WAXS patterns (Figure 3b and c) provided insights into the structure of the growing hollow PtNi/C NPs. The first atomic coordination shells were distinguishable at $t \geq 3$ min (Figure 3c). The peak at 0.249 nm dominated the $G(r)$ signals between $3 \leq t < 4$ min, thereby suggesting the presence of Ni-rich NPs on the carbon support. However, assuming only Ni/C NPs was not sufficient to fully describe the extracted PDFs, most likely because Ni_xB_y and $Ni_xB_yO_z$ phases also formed during the synthesis. At $t = 4$ min, the WAXS data were tentatively fitted with a mixture of Ni and Ni_3B [the calculated theoretical PDFs for different Ni_xB_y phases (NiB, Ni_2B, Ni_3B, Ni_4B_3) are plotted in Figure S6 in the SI]. For $t \geq 4.5$ min, the peak at 0.271 nm became predominant in the PDF patterns, which is in line with the enrichment in Pt evidenced in Figure 1. As shown by Figure S7 in the SI, the $G(r)$ signal at $t = 10$ min and 50 s could be fitted with a single PtNi phase with a lattice parameter of 0.385 nm. At longer times, the PtNi lattice parameter relaxed, in agreement with the continuous loss of Ni atoms from the NPs monitored by X-EDS (Figure 1 and Figure 2) and XPS (Figures S4 and S5). Last, a qualitative observation of the intensity of the Pt−Pt peaks established that the maximum coherence length gradually increased from <0.1 nm before 4.5 min to 2 nm at 60 min.

The transformation of Ni-rich core@Pt-rich shell NPs into hollow PtNi/C NPs was confirmed by operando SAXS measurements. SAXS is a useful tool to probe the structure of the growing NPs in the size domain between several angströms and tens of nanometers. Moreover, as it provides information about the changes in morphology of the NPs during the synthesis, SAXS is complementary to WAXS.[43] The operando SAXS experiments were performed in a separate run using the same experimental setup and synthesis protocol. The background due to the carbon support was eliminated by subtracting the SAXS pattern recorded before the addition of the first $NaBH_4$ solution droplet from the subsequent patterns (see Figures S8 and S9 in the SI).

The variations of the scattering length density (SLD) of the shell and of the core of the NPs (SLD_{shell} and SLD_{core}, respectively) as a function of time are displayed in Figure 4a.

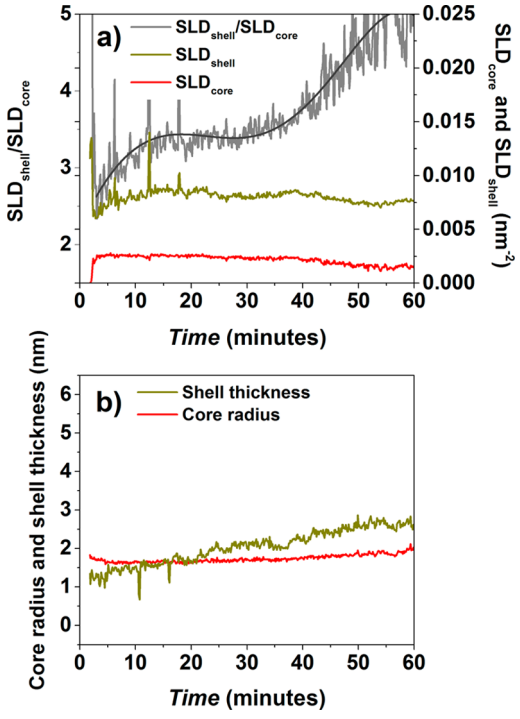

Figure 4. Morphological characterization of the different nanostructures forming during the synthesis of hollow PtNi/C nanoparticles. Variation of the parameters extracted from the fitting of the SAXS data: (a) scattering light density of the core (SLD_{core}), of the shell ((SLD_{shell}) and their ratio, (b) core radius and shell thickness. The solid line in (a) is a fifth order polynomial fit of the SLD_{shell}/SLD_{core} ratio.

Slight changes of the carbon support morphology were observed in the course of the synthesis resulting in uncertainty about scaling factors and absolute values of SLDs. To compensate for these uncertainties, the SLD_{shell}/SLD_{core} ratio (the measurement of the X-ray contrast, and therefore the electron density contrast, between the shell and the core) was plotted in Figure 4a.

DOI: 10.1021/acs.nanolett.7b00119
Nano Lett. 2017, 17, 2447−2453

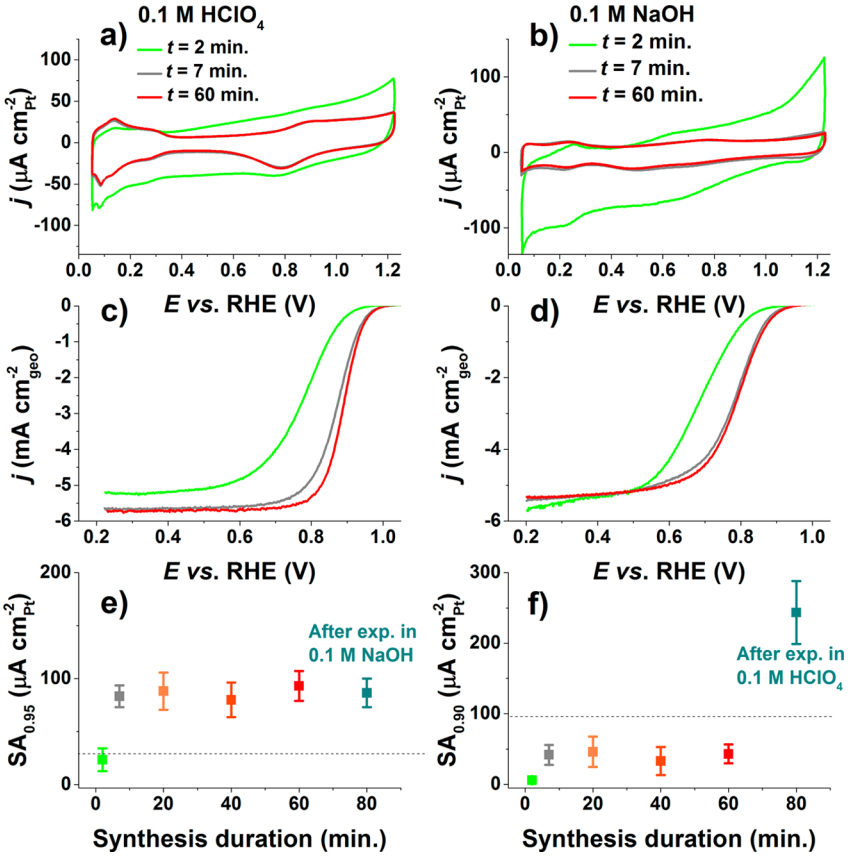

Figure 5. Electrochemical characterization of the different nanostructures forming during the synthesis of hollow PtNi/C nanoparticles. (a, b) Cyclic voltammograms, (c, d) positive-going linear sweep voltammograms, and (e, f) Ohmic drop and mass-transport corrected ORR specific activity. Panels a and b were conducted in Ar-saturated 0.1 M $HClO_4$ or 0.1 M NaOH at v = 0.020 V s^{-1} without rotation of the electrode. Panels c and d were conducted in O_2-saturated 0.1 M $HClO_4$ or 0.1 M NaOH at a potential sweep rate v = 0.005 V s^{-1} and a rotation rate ω = 1600 rpm. Other conditions are at T = 298 ± 1 K. The dashed line corresponds to the value of the specific activity for the ORR of a reference 20 wt % Pt/C measured in the same experimental conditions.

Figure 4b displays the changes of the shell thickness and of the core radius as a function of time. The morphological changes are then described starting from t = 3 min, which corresponds to the time when enough Pt is incorporated in the shell to develop sufficient X-ray contrast between the shell and the core in SAXS measurements. A slight decrease of the radius of the core was observed from 3 < t < 6 min: it is believed not to be physically sound, rather an artifact resulting from the low SLD contrast between the Ni-rich core and the $Ni_xB_yO_z$ shell. For 6 ≤ t < 25 min, a nonmonotonic variation of the shell thickness (from 1.3 to 2.8 nm) was observed in agreement with the enrichment of the surface of the NPs in Pt resulting from galvanic replacement. The core radius remained constant at a size ca. 2 nm during this period. Due to the variations of the individual SLD_{core} and SLD_{shell} values (Figure 4a), the SLD_{shell}/SLD_{core} ratio increased during the first 20 min, flattened out at a value 3.2 ± 0.5 in the time period 20 < t < 35 min, and steeply increased at t ≥ 35 min (Figure 4a). This abrupt variation signs the interdiffusion of Ni atoms initially contained in the core of the NPs into the Pt-rich shell. To the best of our knowledge, this is the first X-ray based physical evidence of a nanoscale Kirkendall effect.

On the basis of the results of WAXS, SAXS, and STEM/X-EDS measurements, a comprehensive formation and growth mechanism for hollow PtNi/C NPs is proposed:

1. 0 < t ≤ 1 min: Ni^{2+} ions are preferentially reduced into solid Ni/C NPs by $NaBH_4$;
2. 1 < t ≤ 2 min: Formation of Ni-rich core@$Ni_xB_yO_z$ shell/C nanostructures;
3. 2 < t ≤ 4 min: Deposition of Pt onto the $Ni_xB_yO_z$ shell via galvanic replacement;
4. 4 < t ≤ 20 min: The metal shell enriches in Pt and thickens. Relaxation of the PtNi lattice parameter;
5. 20 < t ≤ 60 min: Depletion of the core in Ni following the interdiffusion of Ni atoms in the Pt-rich shell. Formation of hollow PtNi/C NPs due to the nanoscale Kirkendall effect and leaching of the Ni-rich cores.

Electrochemical Characterization and Electrocatalytic Activity for the ORR of Intermediates Nanostructures in Acidic and Alkaline Electrolyte. Because Ni-rich core@Pt-rich shell, solid and hollow PtNi NPs supported on high-surface area carbon convey relevance for ORR electrocatalysis, the surface reactivity, and the ORR activity of the different synthesis intermediates were evaluated in acidic (0.1 M $HClO_4$) and alkaline (0.1 M NaOH) electrolyte and benchmarked to those obtained on a commercial Pt/C material. The cyclic voltammograms (CVs) displayed in Figure 5 feature the classical underpotentially deposition of protons (in acid) and water (in alkaline) and surface oxide formation/reduction in the potential region 0.05 < E < 0.4 V and E < 0.6 V vs the reversible hydrogen electrode (RHE), respectively. The

DOI: 10.1021/acs.nanolett.7b00119
Nano Lett. 2017, 17, 2447−2453

CVs provide clear evidence that the surface and near-surface layers are Ni-rich at t = 2 min and Pt-rich at $t \geq 7$ min (Figure 5a and b), in agreement with the findings derived from STEM/X-EDS elemental maps (Figure 1), operando WAXS and SAXS (Figure 3), and XPS (Figure S5) measurements.

The enrichment of the surface and the near-surface layers in Pt translated into increasing specific activity for the ORR both in acidic and alkaline electrolyte, as shown by the positive shift of the half-wave potential and the onset of the ORR (Figure 5c and d). Changes of the specific activity for the ORR measured at E = 0.95 V vs RHE ($SA_{0.95}$) as a function of the synthesis time are plotted in Figure 5e and f. Because of their Ni-rich surface, the specific activity for ORR of the Ni-core@$Ni_xB_yO_z$ shell/C NPs (t = 2 min) was the worst of any synthesis intermediate both in 0.1 M NaOH and 0.1 M $HClO_4$. A 2-fold enhancement of the ORR activity in acidic electrolyte was evidenced for the catalyst sampled at t = 7 min relative to the reference Pt/C material; however, this catalyst performed worse than the benchmark Pt/C in alkaline electrolyte. Finally, a plateau in ORR activity was reached for all synthesis intermediates in acidic electrolyte at $t \geq 7$ min.

To gain more insights into the similar ORR activities, experiments were conducted alternatively in alkaline and acidic electrolyte on the PtNi/C catalyst sampled after 60 min. The results of these measurements showed that the activity for the ORR in alkaline electrolyte could be further improved if ORR kinetics was first measured in acidic and then in alkaline electrolyte (acidic → alkaline, Figure 5f). On the contrary, the specific activity for the ORR in acidic electrolyte was independent of the order of the experiments (alkaline → acidic or acidic → alkaline → acidic, Figure 5e). These results are rationalized based on the formation of a "Pt-skeleton" nanostructure with enhanced ORR activity upon acid leaching, in agreement with former literature findings.[6,7,10] This trend is particularly marked in our study because Ni^{2+} ions released by galvanic replacement and Kirkendall effect recombine with BO_2^- ions produced by BH_4^- hydrolysis and poison the catalytically active sites with $Ni_xB_yO_z$ phases (see eq 5). Last, to gain insights into the durability of the different nanostructures, an accelerated stress test (AST) composed of 5000 potential cycles between 0.60 and 1.00 V vs RHE in 0.1 M $HClO_4$ and T = 353 ± 1 K derived from the Fuel Cell Commercialization of Japan was performed. Because the degradation of Pt-based/C nanoparticles proceeds much faster in alkaline electrolyte,[44] only 500 potential cycles in the same potential range were performed in 0.1 M NaOH. The cyclic voltammograms and the variation of the electrochemically active surface area (ECSA) and of the ORR specific activity during these ASTs are displayed in Figures S10 and S11, respectively. They show (i) slightly decreasing ECSA and specific activity for the ORR values in acidic electrolyte due to the dissolution of Ni atoms and the loss of strain and ligand effects as discussed in our former work,[10] (ii) much harsher degradation but increasing specific activity for the ORR in alkaline electrolyte, in agreement with the findings of Zadick et al.[44] Further discussion of these ASTs results conveys fundamental and applied importance but is beyond the scope of this Letter.

In summary, this study (i) shed fundamental light on the formation and growth mechanism of hollow PtNi/C NPs, (ii) provided the time scale at which elementary steps of the synthesis occur (formation of nickel borides, galvanic replacement, and nanoscale Kirkendall effect) and (iii) opened the possibility to synthesize M-rich core@Pt-rich shell, and solid or hollow alloy NPs supported on carbon simply by controlling the reaction time. We demonstrated that solid Ni/C NPs 5−10 nm in size embedded in $Ni_xB_yO_z$ phases formed during the first 2 min of the synthesis. A transformation of the Ni-rich/C NPs into hollow PtNi/C NPs was evidenced at longer times, Ni-rich core@Pt-rich shell/C NPs being synthesis intermediates. In agreement with the physicochemical characterizations, the specific activity for the ORR in alkaline or acidic electrolytes increased abruptly with the synthesis time and reached a plateau for $t \geq 7$ min. The ORR specific activity in alkaline electrolyte could be improved if the surface Ni atoms were first leached out in acid leading to the formation of a Pt-skeleton nanostructure. Beyond its interest for the synthesis of hollow PtNi/C NPs, this study also introduces a methodology based on advanced electron and X-ray based techniques, which is capable to identify the formation and growth mechanisms of various nanomaterials including preferentially shaped metal NPs, core@shell NPs, onion-like NPs, Janus NPs, or a combination of several of these structures.

■ ASSOCIATED CONTENT

Supporting Information

The Supporting Information is available free of charge on the ACS Publications website at DOI: 10.1021/acs.nanolett.7b00119.

Materials and methods, binding energies of Ni and B standards and $Ni_xB_yO_z$ catalysts, aberration-corrected HR-TEM images and XP spectra of the different nanostructures forming during the synthesis, examples of experimental WAXS and SAXS patterns, calculated PDF for different Ni_xB_y phases, example of PDF refinement of WAXS patterns or fit of SAXS patterns, and cyclic voltammograms and ORR specific activity during accelerated stress testing (PDF)

■ AUTHOR INFORMATION

Corresponding Authors

*E-mail address: (L.D.) laetitia.dubau@lepmi.grenoble-inp.fr.
*E-mail address: (F.M.) frederic.maillard@lepmi.grenoble-inp.fr.

ORCID

Frédéric Maillard: 0000-0002-6470-8900

Author Contributions

R.C. and T.A. contributed equally to this work. All authors performed experimental work, discussed the results, drew conclusions, and have given approval to the final version of the manuscript

Notes

The authors declare no competing financial interest.

■ ACKNOWLEDGMENTS

This work was performed within the framework of the Centre of Excellence of Multifunctional Architectured Materials "CEMAM" no. ANR-10-LABX-44-01. The authors acknowledge the CEA - METSA network for HR-TEM measurements, Dr. Maciej Jankowski and Dr. Helena Isern for their help with the XPS measurements, and the financial support from the French National Research Agency through the HOLLOW project (grant number ANR-14-CE05-0003-01).

DOI: 10.1021/acs.nanolett.7b00119
Nano Lett. 2017, 17, 2447−2453

REFERENCES

(1) Stamenkovic, V. R.; Fowler, B.; Mun, B. S.; Wang, G. F.; Ross, P. N.; Lucas, C. A.; Markovic, N. M. *Science* **2007**, *315*, 493−497.
(2) Xia, B. Y.; Wu, H. B.; Wang, X.; Lou, X. W. *Angew. Chem., Int. Ed.* **2013**, *52* (47), 12337−12340.
(3) Gan, L.; Cui, C.; Heggen, M.; Dionigi, F.; Rudi, S.; Strasser, P. *Science* **2014**, *346* (6216), 1502−1506.
(4) Chen, C.; Kang, Y.; Huo, Z.; Zhu, Z.; Huang, W.; Xin, H. L.; Snyder, J. D.; Li, D.; Herron, J. A.; Mavrikakis, M.; Chi, M.; More, K. L.; Li, Y.; Markovic, N. M.; Somorjai, G. A.; Yang, P.; Stamenkovic, V. R. *Science* **2014**, *343* (6177), 1339−1343.
(5) Zhang, L.; Roling, L. T.; Wang, X.; Vara, M.; Chi, M.; Liu, J.; Choi, S.-I.; Park, J.; Herron, J. A.; Xie, Z.; Mavrikakis, M.; Xia, Y. *Science* **2015**, *349* (6246), 412−416.
(6) Han, B.; Carlton, C. E.; Kongkanand, A.; Kukreja, R. S.; Theobald, B. R.; Gan, L.; O'Malley, R.; Strasser, P.; Wagner, F. T.; Shao-Horn, Y. *Energy Environ. Sci.* **2015**, *8* (1), 258−266.
(7) Dubau, L.; Lopez-Haro, M.; Durst, J.; Guetaz, L.; Bayle-Guillemaud, P.; Chatenet, M.; Maillard, F. *J. Mater. Chem. A* **2014**, *2* (43), 18497−18507.
(8) Dubau, L.; Nelayah, J.; Moldovan, S.; Ersen, O.; Bordet, P.; Drnec, J.; Asset, T.; Chattot, R.; Maillard, F. *ACS Catal.* **2016**, *6* (7), 4673−4684.
(9) Dubau, L.; Lopez-Haro, M.; Durst, J.; Maillard, F. *Catal. Today* **2016**, *262*, 146−154.
(10) Dubau, L.; Asset, T.; Chattot, R.; Bonnaud, C.; Vanpeene, V.; Nelayah, J.; Maillard, F. *ACS Catal.* **2015**, *5* (9), 5333−5341.
(11) Zhao, J.; Chen, W.; Zheng, Y.; Li, X. *J. Power Sources* **2006**, *162* (1), 168−172.
(12) Sun, Q.; Ren, Z.; Wang, R.; Wang, N.; Cao, X. *J. Mater. Chem.* **2011**, *21* (6), 1925−1930.
(13) Wang, J. X.; Ma, C.; Choi, Y.; Su, D.; Zhu, Y.; Liu, P.; Si, R.; Vukmirovic, M. B.; Zhang, Y.; Adzic, R. R. *J. Am. Chem. Soc.* **2011**, *133* (34), 13551−7.
(14) Bae, S. J.; Yoo, S. J.; Lim, Y.; Kim, S.; Lim, Y.; Choi, J.; Nahm, K. S.; Hwang, S. J.; Lim, T. H.; Kim, S. K.; Kim, P. *J. Mater. Chem.* **2012**, *22*, 8820.
(15) Shan, A.; Chen, Z.; Li, B.; Chen, C.; Wang, R. *J. Mater. Chem. A* **2015**, *3* (3), 1031−1036.
(16) Yin, Y. D.; Rioux, R. M.; Erdonmez, C. K.; Hughes, S.; Somorjai, G. A.; Alivisatos, A. P. *Science* **2004**, *304* (5671), 711−714.
(17) Sun, Y.; Mayers, B. T.; Xia, Y. *Nano Lett.* **2002**, *2* (5), 481−485.
(18) Sun, Y.; Xia, Y. *Science* **2002**, *298* (5601), 2176−2179.
(19) Sun, Y.; Mayers, B.; Xia, Y. *Adv. Mater.* **2003**, *15* (7−8), 641−646.
(20) Chen, G.; Xia, D.; Nie, Z.; Wang, Z.; Wang, L.; Zhang, L.; Zhang, J. *Chem. Mater.* **2007**, *19* (7), 1840−1844.
(21) González, E.; Arbiol, J.; Puntes, V. F. *Science* **2011**, *334* (6061), 1377−1380.
(22) Xia, X.; Wang, Y.; Ruditskiy, A.; Xia, Y. *Adv. Mater.* **2013**, *25* (44), 6313−6333.
(23) Sun, Y.; Xia, Y. *J. Am. Chem. Soc.* **2004**, *126* (12), 3892−3901.
(24) *Standard potentials in aqueous solution*; Marcel Dekker, Inc.: New York and Basel, 1985.
(25) Schlesinger, H. I.; Brown, H. C.; Finholt, A. E.; Gilbreath, J. R.; Hoekstra, H. R.; Hyde, E. K. *J. Am. Chem. Soc.* **1953**, *75* (1), 215−219.
(26) Glavee, G. N.; Klabunde, K. J.; Sorensen, C. M.; Hadjapanayis, G. C. *Langmuir* **1992**, *8* (3), 771−773.
(27) Glavee, G. N.; Klabunde, K. J.; Sorensen, C. M.; Hadjipanayis, G. C. *Langmuir* **1993**, *9* (1), 162−169.
(28) Glavee, G. N.; Klabunde, K. J.; Sorensen, C. M.; Hadjipanayis, G. C. *Inorg. Chem.* **1993**, *32* (4), 474−477.
(29) Glavee, G. N.; Klabunde, K. J.; Sorensen, C. M.; Hadjipanayis, G. C. *Langmuir* **1994**, *10* (12), 4726−4730.
(30) Glavee, G. N.; Klabunde, K. J.; Sorensen, C. M.; Hadjipanayis, G. C. *Inorg. Chem.* **1995**, *34* (1), 28−35.
(31) Geng, J.; Jefferson, D. A.; Johnson, B. F. G. *Chem. Commun.* **2007**, *9*, 969−971.
(32) Geng, J.; Jefferson, D. A.; Johnson, B. F. G. *Chem. - Eur. J.* **2009**, *15* (5), 1134−1143.
(33) Arzac, G. M.; Rojas, T. C.; Fernández, A. *ChemCatChem* **2011**, *3* (8), 1305−1313.
(34) Carenco, S.; Portehault, D.; Boissière, C.; Mézailles, N.; Sanchez, C. *Chem. Rev.* **2013**, *113* (10), 7981−8065.
(35) Shen, J.; Li, Z.; Yan, Q.; Chen, Y. *J. Phys. Chem.* **1993**, *97* (32), 8504−8511.
(36) Saida, J.; Inoue, A.; Masumoto, T. *Mater. Sci. Eng., A* **1994**, *179−180*, 577−581.
(37) Kapfenberger, C.; Hofmann, K.; Albert, B. *Solid State Sci.* **2003**, *5* (6), 925−930.
(38) Schaefer, Z. L.; Ke, X.; Schiffer, P.; Schaak, R. E. *J. Phys. Chem. C* **2008**, *112* (50), 19846−19851.
(39) Caputo, R.; Guzzetta, F.; Angerhofer, A. *Inorg. Chem.* **2010**, *49* (19), 8756−8762.
(40) Li, H.; Li, H.; Dai, W.; Qiao, M. *Appl. Catal., A* **2003**, *238* (1), 119−130.
(41) Li, H.; Li, H.; Dai, W. L.; Wang, W.; Fang, Z.; Deng, J. F. *Appl. Surf. Sci.* **1999**, *152* (1), 25−34.
(42) Dubau, L.; Durst, J.; Maillard, F.; Guétaz, L.; Chatenet, M.; André, J.; Rossinot, E. *Electrochim. Acta* **2011**, *56* (28), 10658−10667.
(43) Guinier, A.; Fournet, G. *Small-angle scattering of X-rays*; New York, 1955.
(44) Zadick, A.; Dubau, L.; Sergent, N.; Berthomé, G.; Chatenet, M. *ACS Catal.* **2015**, *5* (8), 4819−4824.

NOTE ADDED AFTER ASAP PUBLICATION

This paper was published on March 30, 2017, before all of the corrections were implemented. The corrected version was reposted on March 31, 2017.

DOI: 10.1021/acs.nanolett.7b00119
Nano Lett. 2017, 17, 2447−2453